npj | Quantum Materials

www.nature.com/npjquantmats

ARTICLE OPEN

Check for updates

Suppressed-moment 2-**k** order in the canonical frustrated antiferromagnet $Gd_2Ti_2O_7$

Joseph A. M. Paddison[1,2,3,4]✉, Georg Ehlers[5], Andrew B. Cairns[3,6], Jason S. Gardner[1], Oleg A. Petrenko[7], Nicholas P. Butch[8], Dmitry D. Khalyavin[4], Pascal Manuel[4], Henry E. Fischer[9], Haidong Zhou[10,11], Andrew L. Goodwin[3] and J. Ross Stewart[4]✉

In partially ordered magnets, order and disorder coexist in the same magnetic phase, distinct from both spin liquids and spin solids. Here, we determine the nature of partial magnetic ordering in the canonical frustrated antiferromagnet $Gd_2Ti_2O_7$, in which Gd^{3+} spins occupy a pyrochlore lattice. Using single-crystal neutron-diffraction measurements in applied magnetic field, magnetic symmetry analysis, inelastic neutron-scattering measurements, and spin-wave modeling, we show that its low-temperature magnetic structure involves two propagation vectors (2-**k** structure) with suppressed ordered magnetic moments and enhanced spin-wave fluctuations. Our experimental results are consistent with theoretical predictions of thermal fluctuation-driven order in $Gd_2Ti_2O_7$, and reveal that inelastic neutron-scattering measurements on powder samples can solve the longstanding problem of distinguishing single-**k** and multi-**k** magnetic structures.

npj Quantum Materials (2021)6:99 ; https://doi.org/10.1038/s41535-021-00391-w

INTRODUCTION

Geometrical frustration is a central theme of condensed-matter physics because it can generate exotic magnetic states. These states can typically be divided into spin liquids, in which frustration inhibits long-range magnetic order, and spin solids, in which perturbations to the dominant frustrated interactions drive magnetic order[1]. Defying this classification, some frustrated magnets exhibit partial magnetic order[2–8]—the coexistence of order and disorder in the same magnetic phase. Magnetic partial order can be driven by fluctuations in an "order-by-disorder" scenario[9], by interactions between emergent degrees of freedom in spin-fragmented states[10–12], or by proximity to a quantum critical point[13], while structural partial order can drive the behavior of materials such as fast-ion conductors[14,15], Pb-based photovoltaics[16,17], and high-pressure elemental phases[18]. To benchmark theories of partially ordered states[9,19,20], experimental determination of the nature of partial magnetic ordering in real materials is crucial.

Materials in which magnetic ions occupy a pyrochlore lattice of corner-sharing tetrahedra provide opportunities for realizing exotic frustrated states[21]. The frustrated pyrochlore antiferromagnet $Gd_2Ti_2O_7$ is a canonical partially ordered system in which magnetic Gd^{3+} ions ($S = 7/2$, $L = 0$) undergo two phase transitions at $T_1 = 1.1$ K and $T_2 = 0.75$ K[22–26]. Both low-temperature ($T \ll T_2$) and intermediate ($T_2 < T < T_1$) phases have magnetic propagation vector $\mathbf{k} = (\frac{1}{2}\frac{1}{2}\frac{1}{2})$[27,28], which is uncommon among rare-earth pyrochlores and suggests exchange interactions extend beyond nearest neighbors[20]. Both magnetic structures are also partially ordered, as shown by the coexistence of magnetic Bragg and diffuse scattering in polarized-neutron scattering measurements[28]. The presence of partial ordering in a magnetic ground state at millikelvin temperatures is highly unusual[21,28]. However, the low-temperature magnetic structure of $Gd_2Ti_2O_7$ has not yet been conclusively solved, for two reasons. First, the large neutron absorption cross-section of natural Gd makes neutron-scattering experiments on large crystals challenging. Second, most experimental probes are unable to distinguish a magnetic structure that orders with a single $\mathbf{k} = (\frac{1}{2}\frac{1}{2}\frac{1}{2})$ wavevector (1-**k** structure) from structures that superpose symmetry-equivalent $\mathbf{k} \in \langle\frac{1}{2}\frac{1}{2}\frac{1}{2}\rangle$ (2-**k**, 3-**k**, and 4-**k** structures). This phenomenon is known as the "multi-**k** problem"[29]. Developing methodologies to solve the multi-**k** problem is of broad relevance, because multi-**k** structures often correspond to noncollinear spin textures with nontrivial topological properties, such as skyrmions, hedgehogs, and vortex crystals (see, e.g., refs. [30–34]).

Figure 1 shows the 1-**k**, 2-**k**, 3-**k**, and 4-**k** magnetic-structure candidates and their space groups. All are partially ordered, but each has a different modulation of the ordered magnetic moment μ_{ord}: the 1-**k** and 4-**k** structures have 25% interstitial paramagnetic sites, whereas 2-**k** and 3-**k** structures have more complicated μ_{ord} modulations. It was proposed in ref. [28] that magnetic diffuse-scattering measurements in the low-temperature phase support a 4-**k** structure with cubic magnetic symmetry. However, this result was called into question by the observation of transverse magnetization in small applied magnetic fields $\mathbf{H} \parallel \langle 112 \rangle$ and $\langle 100 \rangle$, which is inconsistent with cubic symmetry[35,36]. Theory proposes that the ordering is driven by a subtle interplay of energetic and entropic terms[9]. For interaction parameters relevant to $Gd_2Ti_2O_7$, 1-**k** and 4-**k** structures are degenerate, and the 4-**k** structure is stabilized at T_1 by thermal fluctuations in an "order-by-disorder" mechanism. The same model predicts a second phase transition at T_2 into a 2-**k** ground state[9]. These striking predictions have awaited a conclusive experimental test.

[1]Materials Science & Technology Division, Oak Ridge National Laboratory, Oak Ridge, TN 37831, USA. [2]Churchill College, University of Cambridge, Storey's Way, Cambridge CB3 0DS, UK. [3]Inorganic Chemistry Laboratory, University of Oxford, South Parks Road, Oxford OX1 3QR, UK. [4]ISIS Neutron and Muon Source, Rutherford Appleton Laboratory, Didcot OX11 0QX, UK. [5]Neutron Technologies Division, Oak Ridge National Laboratory, Oak Ridge, TN 37831, USA. [6]Department of Materials, Imperial College London, Royal School of Mines, Exhibition Road, London SW7 2AZ, UK. [7]Department of Physics, University of Warwick, Coventry CV4 7AL, UK. [8]NIST Center for Neutron Research, National Institute of Standards and Technology, Gaithersburg, MD 20899, USA. [9]Institut Laue-Langevin, 71 avenue des Martyrs, CS 20156, 38042 Grenoble Cédex 9, France. [10]Department of Physics and Astronomy, University of Tennessee, Knoxville, TN 37996, USA. [11]National High Magnetic Field Laboratory, Florida State University, Tallahassee, FL 32310, USA. ✉email: paddisonja@ornl.gov; ross.stewart@stfc.ac.uk

In this article, we experimentally determine the nature of partial magnetic order in $Gd_2Ti_2O_7$ using neutron-scattering measurements of isotopically enriched powder and single-crystal samples, combined with symmetry analysis and spin-wave calculations. We show that the low-temperature state of $Gd_2Ti_2O_7$ is actually 2-**k**, in agreement with theory[9] but in contradiction with the interpretation of previous experiments[28]. Remarkably, inelastic neutron-scattering (INS) experiments on a powder sample unambiguously distinguish between *n*-**k** structures, demonstrating that neither single crystals nor symmetry-breaking perturbations such as applied field are prerequisite to solve the multi-**k** problem.

Our paper is structured as follows. We first present single-crystal neutron-diffraction measurements in applied magnetic field that suggest non-cubic magnetic symmetry. We then perform a comprehensive symmetry analysis of candidate magnetic structures. Finally, we show that only a partially ordered 2-**k** structure is consistent with low-temperature INS data. We conclude by discussing the general implications of our study for understanding partially ordered states and solving multi-**k** structures.

RESULTS

Evidence for field-dependent magnetic domain population

An example of the multi-**k** problem[29] is that measurements of magnetic Bragg intensities in zero applied magnetic field do not directly distinguish the structures shown in Fig. 1, due to spherical averaging in powder samples or averaging over degenerate magnetic domains in single crystals. To address this problem, we performed single-crystal neutron-diffraction measurements and applied a weak magnetic field $\mathbf{H}\|[1\bar{1}0]$ to break the domain degeneracy at $T = 0.07$ K after zero-field cooling. Domains of the cubic 4-**k** structure are related only by translational and time-reversal symmetries and hence appear identical to neutrons, whereas domains of other *n*-**k** structures are related by rotational symmetries and hence have different diffraction patterns. A field-induced domain imbalance is therefore expected to leave the diffraction pattern unchanged only if the low-temperature structure is 4-**k**.

The magnetic field dependence of selected magnetic Bragg intensities is shown in Fig. 2. Magnetic Bragg peaks in the (*hhl*) plane disappear in small applied field $0.2 \leq \mu_0 H \leq 0.5$ T, while magnetic Bragg peaks outside the (*hhl*) plane become more intense. These observations are incompatible with the cubic 4-**k** structure, unless the applied field actually causes a magnetic phase transition rather than a domain imbalance. This scenario occurs in $Er_2Ti_2O_7$[37], but appears unlikely in $Gd_2Ti_2O_7$, in which no experimental signature of such a phase transition is observed in either specific heat[25] or torque magnetometry[35] measurements at base temperature and for $\mu_0\mathbf{H}\|\langle 110\rangle$ of less than 2 T. The field-induced uniform magnetization is also too small to suppress antiferromagnetic Bragg peaks significantly ($M = 0.2\,\mu_B$ for $\mu_0 H = 0.2$ T[26,36]) and so need not be considered. Moreover, our conclusion is unaffected by the significant neutron absorption of our single-crystal sample, because it is indicated by the field dependence of the peak intensities, and not by comparing the intensities of different peaks at the same field. These observations provide evidence against the cubic 4-**k** structure; however, they do not distinguish between non-cubic structures such as 1-**k** and 2-**k** candidates.

Magnetic symmetry analysis

To constrain further the low-temperature magnetic structure, we reinterpret published powder neutron-diffraction data measured at 0.25 K (from ref. [28]) using a comprehensive symmetry analysis.

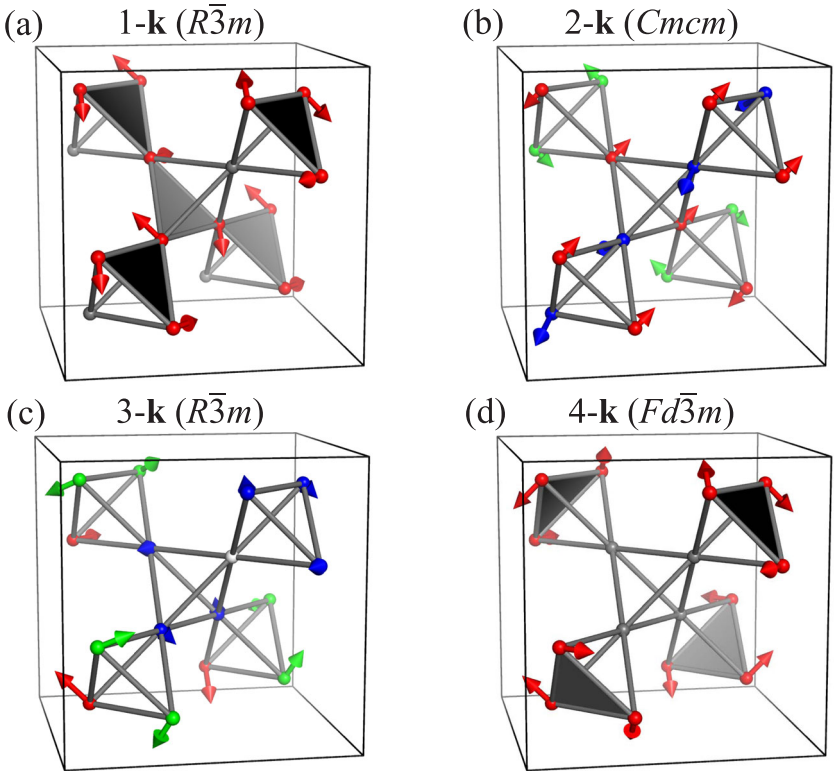

Fig. 1 Candidate magnetic structures. Basic candidate structures for $Gd_2Ti_2O_7$, showing **a** 1-**k**, **b** 2-**k**, **c** 3-**k**, and **d** 4-**k** structures. The symmetry of each structure is labeled. A single crystallographic unit cell is shown in each case; spin orientations are reversed in adjacent unit cells because of the $\mathbf{k} = (\frac{1}{2}\frac{1}{2}\frac{1}{2})$ propagation vector. Spin directions are shown as arrows with lengths proportional to the ordered moment magnitude μ_{ord}, and the spin planes of triangular plaquettes for the 1-**k** and 4-**k** structures are shaded gray. Arrows of different colors indicate symmetry-inequivalent magnetic sites, and paramagnetic sites with zero μ_{ord} in **a**, **c**, and **d** are shown as gray spheres.

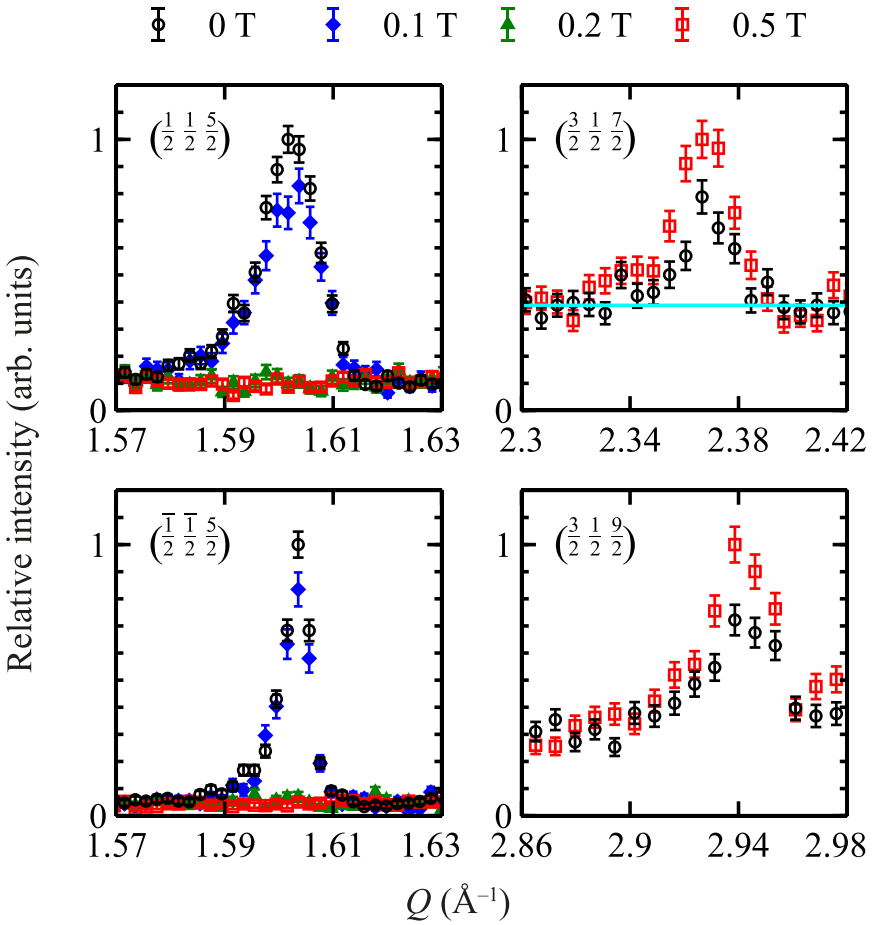

Fig. 2 Field dependence of single-crystal magnetic Bragg scattering. Relative intensities of selected single-crystal magnetic Bragg peaks at different values of applied magnetic field $\mathbf{H}\|[1\bar{1}0]$ at $T = 0.07$ K. Magnetic Bragg peaks are labeled in each panel and applied fields $\mu_0\mathbf{H}$ are as labeled above the panels. To emphasize the field dependence, intensities are normalized such that the maximum intensity in each panel is unity. Error bars represent one standard deviation. For the $(\frac{3}{2}\frac{3}{2}\frac{7}{2})$ peak, the integrated intensity is 0.11(2) units for $H = 0$ and 0.22(2) units for $\mu_0 H = 0.5$ T, consistent with the expected doubling; the estimated background is shown as a light blue line.

Figure 3 shows the magnetic diffraction data, with nuclear Bragg peaks subtracted, as a function of wavevector magnitude $Q = |\mathbf{Q}| = 2\pi/d$. The possible magnetic irreducible representations for the $Fd\bar{3}m$ space group (with origin choice 2) are denoted L_{1+}, L_{2+}, L_{3+}, L_{1-}, and L_{3-} in Miller and Love's notation[38]. Importantly, this analysis makes no assumptions about the nature of the phase transition at T_2 (continuous or discontinuous), because we do not assume an intermediate-temperature parent structure, but instead consider the paramagnetic space group as the parent symmetry. Previous studies have shown that nearly all the features of the data can be modeled using a single irrep, L_{1+}, which yields the fit shown in Fig. 3a[27,28]. The L_{1+} model is the best currently available and generates the four basic n-**k** structures shown in Fig. 1. Crucially, however, the $(\frac{1}{2}\frac{1}{2}\frac{1}{2})$ magnetic Bragg peak observed in the 0.25 K data is absent for the L_{1+} model (inset to Fig. 3a). This peak appears at T_2[28], and is accompanied by a large specific-heat anomaly observed in several different samples[24,25], suggesting that it is intrinsic and sample-independent. Hence, while the L_{1+} irrep is the main contributor to the low-temperature magnetic structure, at least one other irrep must also be present. We therefore investigated the four possible combinations of L_{1+} with one other irrep. Only the (L_{1+}, L_{3-}) and (L_{1+}, L_{3+}) irrep pairs allow nonzero intensity of the $(\frac{1}{2}\frac{1}{2}\frac{1}{2})$ peak and so are candidates. For each irrep pair, a given set of magnetic distortion-mode amplitudes[39,40] yields several magnetic structures with identical Bragg profiles. Accordingly, we treated the magnetic distortion-mode amplitudes as free parameters that we optimized against our diffraction data. Figure 3 compares fits to diffraction data for the single-irrep L_{1+} model with the two-irrep (L_{1+}, L_{3-}) and (L_{1+}, L_{3+}) models. The two-irrep models yield nonzero intensity of the weak $(\frac{1}{2}\frac{1}{2}\frac{1}{2})$ peak—and slightly improved overall fits to the data—by increasing the number of free parameters as indicated in Fig. 3. Unfortunately, the inclusion of an additional irrep also increases the number of candidate structures from four to 32, all of which are consistent with the diffraction data. The magnetic space groups, mode amplitudes, and ordered-moment lengths for these structures are given in Supplementary Tables 1–3. To compress this search space, we apply a physical criterion that no site should have $\mu_{ord} > 7.0$ μ_B—the maximum value for $S = 7/2$ Gd^{3+} ions—which reduces the number of candidate structures to eight. Importantly, this criterion rules out all 3-**k** structures, so we do not consider these further. Four of the eight remaining structures are monoclinic (L_{1+}, L_{3-}) variants of the 1-**k** structure, in which paramagnetic spins order with a small μ_{ord}[28]. However, these structures are disfavored by symmetry because the L_{3-} irrep is not a symmetry-allowed secondary order parameter (SOP) of the 1-**k** structure[39,40]. The other four structures comprise three 2-**k** and one 4-**k**. Of these, the second irrep is a symmetry-allowed SOP in only one candidate—a (L_{1+}, L_{3+}) 2-**k** structure. This structure satisfies the moment-length criterion, unlike the single-irrep 2-**k** structure that was therefore discounted in previous work[28,41]. Hence, while the (L_{1+}, L_{3+}) 2-**k**

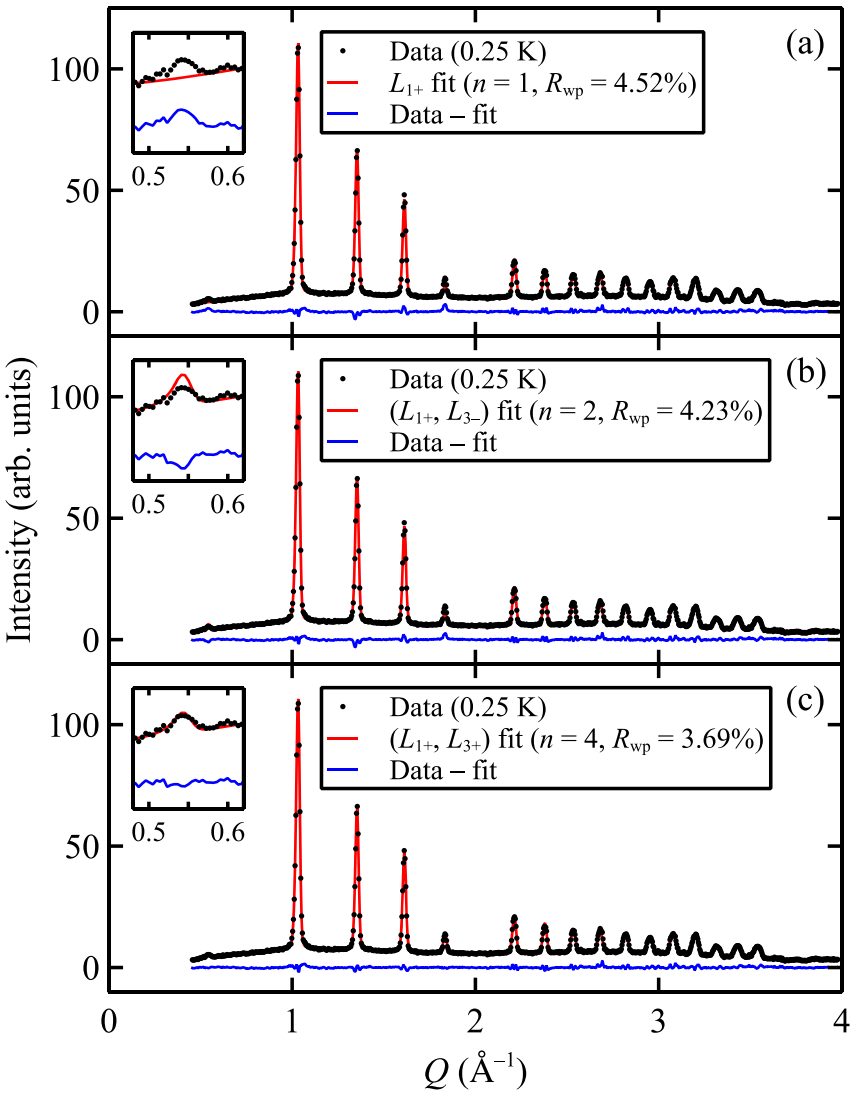

Fig. 3 Powder neutron-diffraction data and magnetic Rietveld refinements. Experimental powder neutron-diffraction data (from ref. [28], $\lambda = 2.42$ Å) in the low-temperature phase (0.25 K) and Rietveld fits for **a** the L_{1+} irrep, **b** the (L_{1+}, L_{3-}) irrep pair, and **c** and the (L_{1+}, L_{3+}) irrep pair. Experimental data are shown as black points, fits as red lines, and data—fit as blue lines. For each model, the number of free parameters (magnetic distortion modes) n and the goodness-of-fit metric R_{wp} are shown. The insets show the $(\frac{1}{2}\frac{1}{2}\frac{1}{2})$ magnetic Bragg peak on an expanded scale.

structure has the same magnetic Bragg profile as other candidates, physical and symmetry arguments favor it.

Inelastic neutron scattering and spin-wave analysis

While powder-averaged Bragg scattering cannot directly distinguish n-**k** structures, this limitation need not apply to the powder-averaged excitation spectrum. We therefore turn to powder INS experiments with high energy resolution (≈0.025 meV FWHM). Figures 4a, b show background-subtracted powder INS data in the intermediate phase (0.77 K) and the low-temperature phase (~0.05 K), respectively. The magnetic scattering at 0.77 K is broad in Q and E. By contrast, the low-temperature data show two relatively flat modes at energies of approximately 0.06 meV and 0.17 meV. Additional INS measurements on a thin piece of our single crystal show that the background-subtracted single-crystal scattering integrated over $(h, k, l) = (0 \pm 1, 0 \pm 1, \frac{3}{2} \pm \frac{1}{2})$ qualitatively resembles the powder data (Fig. 4c).

We use linear spin-wave theory to test candidate magnetic structures against the low-temperature excitation spectrum. The minimal spin Hamiltonian for $Gd_2Ti_2O_7$ is given by

$$H = J_1 \sum_{\langle i,j \rangle} \mathbf{S}_i \cdot \mathbf{S}_j + J_2 \sum_{\langle\langle i,j \rangle\rangle} \mathbf{S}_i \cdot \mathbf{S}_j + D \sum_i (S_i^z)^2 + H_{\mathrm{dip}}, \quad (1)$$

where J_1 and J_2 denote Heisenberg exchange interactions between nearest neighbor and next-nearest neighbor spin pairs, which are denoted by angle brackets $\langle\, \rangle$ and $\langle\, \langle\, \rangle\, \rangle$, respectively; D is a single-ion anisotropy term that arises from mixture of the excited $^6P_{7/2}$ atomic state into the $^8S_{7/2}$ ground state[42]; and

$$H_{\mathrm{dip}} = D_{\mathrm{dip}} r_{\mathrm{nn}}^3 \sum_{i,j} \frac{\mathbf{S}_i \cdot \mathbf{S}_j - 3(\mathbf{S}_i \cdot \hat{\mathbf{r}}_{ij})(\mathbf{S}_j \cdot \hat{\mathbf{r}}_{ij})}{r_{ij}^3} \quad (2)$$

is the long-ranged magnetic dipolar interaction including contributions from all spin pairs i, j, whose energy scale $D_{\mathrm{dip}}S(S+1) = 0.84$ K is fixed by S and the nearest-neighbor distance $r_{\mathrm{nn}} = 3.60$ Å[22]. We assume the literature value of $J_1 S(S+1) = 4.8$ K[22] and include a small ferromagnetic $J_2 = -0.04 J_1$ to stabilize $\mathbf{k} = (\frac{1}{2}\frac{1}{2}\frac{1}{2})$ ordering[9,20,22]; however, the spin-wave spectrum is not strongly

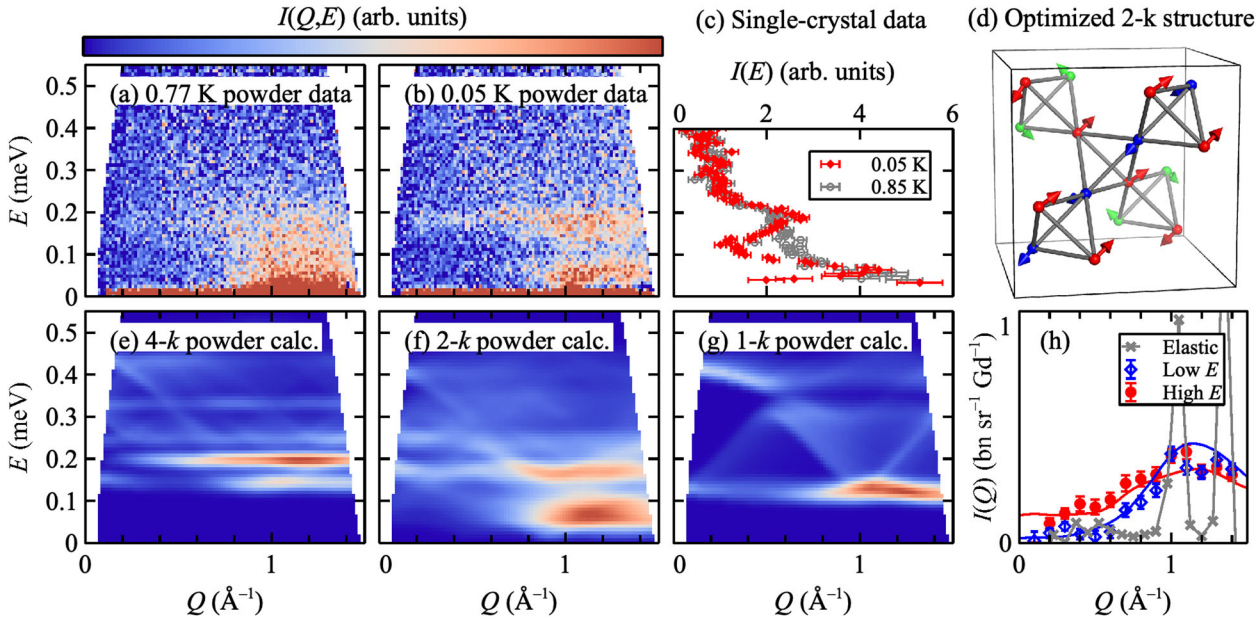

Fig. 4 Inelastic neutron-scattering data and spin-wave models. a Inelastic neutron scattering data collected on a powder sample in the intermediate phase (0.77 K). **b** Powder INS data collected in the low-temperature phase (~0.05 K). **c** Single-crystal INS data integrated over $(h,k,l) = (0\pm1, 0\pm1, \frac{3}{2}\pm\frac{1}{2})$ in the low-temperature phase (0.05 K, solid red diamonds) and intermediate phase (0.85 K, empty gray circles). Error bars represent one standard deviation. **d** Optimized 2-**k** magnetic structure. **e** Powder-averaged linear spin-wave theory (LSWT) calculation for the L_{1+} 4-**k** structure. **f** Powder LSWT calculation for the optimized (L_{1+}, L_{3+}) 2-**k** structure discussed in the text. **g** Powder LSWT calculation for the L_{1+} 1-**k** structure. **h** Powder INS data and spin-wave calculations at 0.05 K. Experimental data are given in absolute intensity units by normalization to the nuclear Bragg profile. Gray crosses show the measured elastic line ($|E| < 0.03$ meV) with the incoherent scattering cross-section subtracted, empty blue diamonds show the measured low-E mode ($0.03 \le E < 0.12$ meV), and filled red circles show the measured high-E mode ($0.12 \le E \le 0.21$ meV). Spin-wave calculations for low-E and high-E modes are shown as blue and red lines, respectively, and have been vertically scaled by the same factor to match the experimental data.

affected by choosing different small values of J_2. Electron-spin resonance (ESR) experiments find an easy-plane anisotropy that favors spin alignment perpendicular to local ⟨111⟩ axes[42]; we take $DS^2 = 1.5$ K to match our INS data optimally. As an independent check on these interaction parameters, we performed measurements of the paramagnetic ($T > T_1$) diffuse scattering using the D4 diffractometer at the ILL[43,44], and find these are consistent with Monte Carlo simulations[45] of the paramagnetic diffuse scattering for our parameter values (Supplementary Fig. 1).

A prerequisite for spin-wave modeling is that the magnetic structure is a local energy minimum of Eq. (1). We therefore tested which of the eight candidate structures are proximate to energy minima by iteratively aligning each spin with its mean field and checking for stability via the absence of imaginary spin-wave modes. Two candidate structures—one 2-**k** and one 4-**k**—are locally stable; both derive from the (L_{1+}, L_{3+}) irrep pair that yields the best fit to diffraction data (Fig. 3c). By contrast, all candidate 1-**k** structures with nonzero interstitial μ_{ord} are unstable. Figure 4d shows the optimized (L_{1+}, L_{3+}) 2-**k** structure, which resembles the refined structure (Supplementary Fig. 2 and Supplementary Table 4). Compared to the L_{1+} 2-**k** structure shown in Fig. 1b, it has canted magnetic moments with more uniform magnitudes, $\mu_{\text{ord}}/\mu_B \in \{6.1(1), 4.6(1), 6.2(1)\}$ in a 1:1:2 ratio. However, the suppression of μ_{ord} compared to its theoretical value of 7.0 μ_B indicates partial ordering. Figure 4e–g shows the calculated spin-wave spectra for the L_{1+} 4-**k**, (L_{1+}, L_{3+}) 2-**k**, and L_{1+} 1-**k** structures, respectively. The (L_{1+}, L_{3+}) 4-**k** structure involves weak ordering of the 25% of spins that are paramagnetic in the L_{1+} 4-**k** structure; however, the spectra for both these structures are very similar and we show only the latter. The 1-**k** and 4-**k** calculations strongly disagree with the 0.05 K experimental data. By contrast, the 2-**k** calculation reproduces well the experimental data, most importantly the prominent low-energy (~0.06 meV) mode that is absent for the other candidates. This key qualitative observation is not affected by different choices of interaction parameters in the physically appropriate regime $J > D \gg J_2$. The Q dependences of the low-E ($0.03 \le E < 0.12$ meV) and high-E ($0.12 \le E \le 0.21$ meV) modes shown in Fig. 4h confirm agreement between the 2-**k** calculation and the experimental data. We therefore conclude that the (L_{1+}, L_{3+}) 2-**k** structure is the correct low-temperature model.

Investigation of spin-lattice coupling

The 2-**k** structure has orthorhombic symmetry (magnetic space group C_amcm), which is therefore expected to drive a crystallographic distortion via spin-lattice coupling. To test this hypothesis, we performed high-resolution powder neutron-diffraction measurements with $\Delta Q/Q = 5 \times 10^{-5}$ on the HRPD instrument at ISIS[46,47]. However, our data do not show visible peak splitting [Supplementary Fig. 2], and while a statistically significant rhombohedral distortion could be refined, orthorhombic refinements were inconclusive due to their increased number of parameters. This suggests that spin-lattice coupling in $Gd_2Ti_2O_7$ is too weak to yield an observable orthorhombic distortion in our measurements. Further experiments, such as NMR or Mössbauer spectroscopy, may allow the expected distortion to be observed, but the requirement for <0.7 K temperatures presents experimental challenges.

DISCUSSION

Our experimental result that the low-temperature structure of $Gd_2Ti_2O_7$ is 2-**k** confirms state-of-the-art theoretical predictions[9]. However, it contradicts a previous experimental study[28], which proposed a 4-**k** low-temperature structure based on analysis of low-temperature magnetic diffuse scattering. This study did not consider 2-**k** structures, because the single-irrep 2-**k** structure is

unphysical and two-irrep 2-**k** structures were not identified. It also assumed that ordered sites contribute no diffuse scattering. This assumption is incorrect, however, because spin-wave scattering from ordered sites contributes to the energy-integrated diffuse intensity. In general, the magnetic Bragg intensity is proportional to $(\mu_{\rm ord}/\mu_{\rm B})^2$ and the total magnetic intensity is proportional to $g^2S(S+1)$ for a spin-only ion. For a fully ordered system, $\mu_{\rm ord}/\mu_{\rm B} = gS$, so that spin-wave scattering would comprise $1/(S+1) = 22\%$ of the total intensity for $S = 7/2$. By contrast, partially ordered $Gd_2Ti_2O_7$ has $\mu_{\rm ord}/\mu_{\rm B} < gS$. Combining the refined values of $\mu_{\rm ord}$ with the total-moment sum rule, we estimate that low-temperature diffuse scattering comprises 46(2)% of the total intensity. The inelastic scattering ($E > 0.03$ meV) shows clear Q dependence that is fully reproduced by the spin-wave calculation, whereas the elastic scattering ($|E| < 0.03$ meV) is weak and essentially flat away from Bragg peaks. Therefore, the low-temperature magnetic diffuse scattering arises primarily from enhanced spin-wave fluctuations, and not from static spin disorder or quasielastic (paramagnetic) spin fluctuations.

Our neutron-scattering experiments, magnetic symmetry analysis, and spin-wave modeling reveal that the low-temperature magnetic structure of $Gd_2Ti_2O_7$ is 2-**k**, solving a longstanding problem in the field of frustrated pyrochlore oxides. The 2-**k** structure does not contain any entirely paramagnetic sites, and the increase in uniformity of the ordered-moment magnitudes likely stabilizes it over higher-symmetry 1-**k** and 4-**k** candidates. Nevertheless, the 2-**k** structure remains partially ordered, because magnetic-moment magnitudes are modulated and suppressed by up to 35% compared to their fully ordered value, while spin-wave fluctuations are enhanced. The magnetic ground state thus combines partial ordering with a multi-**k** structure—an exotic combination that, to the best of our knowledge, has not been observed in any other material with localized magnetic moments. Its existence in $Gd_2Ti_2O_7$ is especially remarkable because the large value of the spin quantum number and absence of orbital angular momentum for Gd^{3+} ions suggests that quantum effects are weak. Instead, the enhancement of spin fluctuations may be related to the near-degeneracy of 2-**k** and 4-**k** states that results from the interplay of frustrated exchange interactions with magnetic anisotropy and long-ranged dipolar interactions.

While our study has focused on the low-temperature ground state, our results also shed light on the intermediate phase. Theory predicts that a 4-**k** structure is stabilized by thermal fluctuations at T_1 for our interaction parameters, before transitioning to a 2-**k** ground state at T_2[9]. This prediction is consistent with the experimental observation that the $(\frac{1}{2}\frac{1}{2}\frac{1}{2})$ magnetic Bragg peak is absent in the intermediate phase[28], because the irreps required to generate this peak are not symmetry-allowed SOPs for the 4-**k** structure. Moreover, our INS data in the intermediate phase show only broad inelastic features (Fig. 4a), consistent with the observation of quasielastic scattering in neutron-spin-echo experiments in the intermediate phase[48]. A reduction in spin-wave scattering intensity is expected due to elevated temperature ($T = 0.75T_1$), which suppresses the refined value of the ordered magnetic moment to 2.65(3) $\mu_{\rm B}$ per ordered Gd at 0.77 K, for a 4-**k** model [Supplementary Fig. 4]. However, the near-complete suppression of spin-wave intensity of the intermediate phase may hint at the presence of purely paramagnetic sites in a 4-**k** structure. Such sites would contribute a broad continuum of magnetic scattering, as observed in our INS data (Fig. 4a), and may also suppress propagating spin-wave excitations, similar to the effect of paramagnetic impurities[49]. Modeling these effects in the intermediate phase would provide a possible avenue for future work.

Perhaps the most general implication of our study is that single-**k** and multi-**k** structures can be unambiguously distinguished using inelastic neutron-scattering experiments on powder samples in zero applied field. In contrast to previous approaches[50–52], this approach requires neither single crystal samples nor the application of external fields that explicitly break the symmetry. We anticipate that this approach will be widely applicable, and will help identify and understand multi-**k** structures where noncoplanar spin textures have nontrivial topologies[30–34].

METHODS

Single-crystal sample growth

A single crystal was prepared by the floating-zone image furnace method[53,54] and was 99.4% enriched with ^{160}Gd to minimize neutron absorption by ^{155}Gd and ^{157}Gd.

Neutron diffraction experiments

Single-crystal neutron-diffraction measurements were performed using the WISH time-of-flight diffractometer at ISIS[55] on $a = 10\,{\rm mm}^3$ piece cut from our single crystal. This sample was aligned with the (*hhl*) scattering plane horizontal, and loaded within a dilution refrigerator and magnet, with the magnetic field along the vertical $[1\bar{1}0]$ direction. Details of the previously published powder neutron-diffraction measurements are given in ref. [28].

Inelastic neutron-scattering experiments

Powder inelastic neutron-scattering experiment measurements were performed using the DCS spectrometer at NIST[56] with an incident wavelength of 8.0 Å. An approximately 0.2 g portion of the same isotopically enriched powder sample studied in ref. [28] was loaded in a Cu foil and wrapped around the circumference of a cylindrical Cu container, to minimize neutron absorption. Single-crystal inelastic neutron-scattering experiments measurements were performed on a thin piece of our crystal using the CNCS instrument at ORNL with an incident wavelength of 9.0 Å. The samples were cooled using dilution refrigerators.

Magnetic structure refinement

Magnetic refinements to the powder neutron-diffraction data shown in Fig. 3 were performed using the Topas Academic software[57]. Lattice and profile parameters (peak shape, zero offset, and background) were obtained by Pawley refinement to the experimental magnetic Bragg profile, and the intensity scale factor was obtained from refinement to the nuclear Bragg profile. Refinement of an overall Debye–Waller parameter yielded a positive value, indicating that absorption is not a major problem for the powder sample. For each irrep or pair of irreps, the magnetic distortion-mode amplitudes were then refined to the experimental magnetic Bragg profile, keeping lattice, scale, and profile parameters fixed. To identify different sets of mode amplitudes with identical fit quality (degenerate solutions), multiple refinements were performed with different initial values of the mode amplitudes. For the (L_{1+}, L_{3-}) irrep pair, we identified two degenerate sets of mode amplitudes, A and B, given in Supplementary Table 1. For the (L_{1+}, L_{3+}) irrep pair, we identified the four degenerate sets of mode amplitudes C–F given in Supplementary Table 2. By combining these sets of mode amplitudes with the *n*-**k** structures using the Isodistort software[39,40], we identified 32 candidate magnetic structures. The magnetic space groups, mode amplitudes, and ordered-moment magnitudes for these structures are given in Supplementary Table 3.

Spin-wave calculations

Spin-wave calculations shown in Fig. 4e–h were performed using the SpinW software package[58]. For each candidate magnetic structure, we generated a magnetic unit cell containing $2\times2\times2$ crystallographic unit cells (128 ordered magnetic moments); this "supercell" approach is necessary to calculate spin-wave spectra of multi-**k** structures. The candidate structures were then optimized by iteratively aligning the orientation of each ordered magnetic moment with its mean field. The magnetic dipolar interaction was evaluated by direct summation to a maximum interatomic distance of 40 Å. We checked that the optimized magnetic structure and excitation spectrum remained stable to summations over longer distances (up to 100 Å), indicating that satisfactory convergence was achieved. The optimized and refined (L_{1+}, L_{3+}) 2-**k** structures are given in Supplementary Table 4, and their calculated magnetic neutron-diffraction patterns match closely as shown in Supplementary Fig. 3. The calculated spin-wave spectra were powder

averaged numerically using Fibonnaci spherical integration with 987 points on the sphere, multiplied by the squared magnetic form factor of Gd^{3+}, and convolved with a Gaussian with FWHM of 0.025 meV to match the energy resolution of the experimental data.

DATA AVAILABILITY

The datasets generated during and/or analyzed during the current study are available from the corresponding author on reasonable request.

CODE AVAILABILITY

Custom codes generated during the current study are available from the corresponding author on reasonable request.

Received: 3 November 2020; Accepted: 25 May 2021;
Published online: 09 December 2021

REFERENCES

1. Moessner, R. & Ramirez, A. P. Geometrical frustration. *Phys. Today* **59**, 24–29 (2006).
2. Movshovich, R., Jaime, M., Mentink, S., Menovsky, A. A. & Mydosh, J. A. Second low-temperature phase transition in frustrated UNi_4B. *Phys. Rev. Lett.* **83**, 2065–2068 (1999).
3. Greedan, J. E., Wiebe, C. R., Wills, A. S. & Stewart, J. R. Neutron-scattering studies of the geometrically frustrated spinel $LiMn_2O_4$. *Phys. Rev. B* **65**, 184424 (2002).
4. Zheng, X. G. et al. Coexistence of long-range order and spin fluctuation in geometrically frustrated clinoatacamite $Cu_2Cl(OH)_3$. *Phys. Rev. Lett.* **95**, 057201 (2005).
5. Rule, K. C. et al. Polarized inelastic neutron scattering of the partially ordered $Tb_2Sn_2O_7$. *Phys. Rev. B* **76**, 212405 (2007).
6. Cao, G., Durairaj, V., Chikara, S., Parkin, S. & Schlottmann, P. Partial antiferromagnetism in spin-chain $Sr_5Rh_4O_{12}$, $Ca_5Ir_3O_{12}$, and Ca_4IrO_6 single crystals. *Phys. Rev. B* **75**, 134402 (2007).
7. Ehlers, G., Ritter, C., Stewart, J. R., Hillier, A. D. & Maletta, H. Phase transition of geometrically frustrated TbNiAl in a magnetic field. *Phys. Rev. B* **75**, 024420 (2007).
8. Hayes, T. J. et al. Coexistence of the long-range and short-range magnetic order components in $SrEr_2O_4$. *Phys. Rev. B* **84**, 174435 (2011).
9. Javanparast, B., Hao, Z., Enjalran, M. & Gingras, M. J. P. Fluctuation-driven selection at criticality in a frustrated magnetic system: the case of multiple-**k** partial order on the pyrochlore lattice. *Phys. Rev. Lett.* **114**, 130601 (2015).
10. Brooks-Bartlett, M. E., Banks, S. T., Jaubert, L. D. C., Harman-Clarke, A. & Holdsworth, P. C. W. Magnetic-moment fragmentation and monopole crystallization. *Phys. Rev. X* **4**, 011007 (2014).
11. Paddison, J. A. M. et al. Emergent order in the kagome ising magnet $Dy_3Mg_2Sb_3O_{14}$. *Nat. Commun.* **7**, 13842 (2016).
12. Petit, S. et al. Observation of magnetic fragmentation in spin ice. *Nat. Phys.* **12**, 746–750 (2016).
13. Pfleiderer, C. et al. Partial order in the non-fermi-liquid phase of MnSi. *Nature* **427**, 227–231 (2004).
14. Rice, M. J., Strässler, S. & Toombs, G. A. Superionic conductors: theory of the phase transition to the cation disordered state. *Phys. Rev. Lett.* **32**, 596–599 (1974).
15. Keen, D. A., Hull, S., Hayes, W. & Gardner, N. J. G. Structural evidence for a fast-ion transition in the high-pressure rocksalt phase of silver iodide. *Phys. Rev. Lett.* **77**, 4914–4917 (1996).
16. Weller, M. T., Weber, O. J., Henry, P. F., Di Pumpo, A. M. & Hansen, T. C. Complete structure and cation orientation in the perovskite photovoltaic methylammonium lead iodide between 100 and 352 K. *Chem. Commun.* **51**, 4180–4183 (2015).
17. Eames, C. et al. Ionic transport in hybrid lead iodide perovskite solar cells. *Nat. Commun.* **6**, 7497 (2015).
18. Gregoryanz, E. et al. Structural diversity of sodium. *Science* **320**, 1054–1057 (2008).
19. Chern, G.-W., Moessner, R. & Tchernyshyov, O. Partial order from disorder in a classical pyrochlore antiferromagnet. *Phys. Rev. B* **78**, 144418 (2008).
20. Wills, A. S. et al. Magnetic ordering in $Gd_2Sn_2O_7$: the archetypal Heisenberg pyrochlore antiferromagnet. *J. Phys* **18**, L37 (2006).
21. Gardner, J. S., Gingras, M. J. P. & Greedan, J. E. Magnetic pyrochlore oxides. *Rev. Mod. Phys.* **82**, 53–107 (2010).
22. Raju, N. P., Dion, M., Gingras, M. J. P., Mason, T. E. & Greedan, J. E. Transition to long-range magnetic order in the highly frustrated insulating pyrochlore antiferromagnet $Gd_2Ti_2O_7$. *Phys. Rev. B* **59**, 14489–14498 (1999).
23. Ramirez, A. P. et al. Multiple field-induced phase transitions in the geometrically frustrated dipolar magnet: $Gd_2Ti_2O_7$. *Phys. Rev. Lett.* **89**, 067202 (2002).
24. Bonville, P. et al. Low temperature magnetic properties of geometrically frustrated $Gd_2Sn_2O_7$ and $Gd_2Ti_2O_7$. *J. Phys* **15**, 7777 (2003).
25. Petrenko, O. A., Lees, M. R., Balakrishnan, G. & Paul, D. M. Magnetic phase diagram of the antiferromagnetic pyrochlore $Gd_2Ti_2O_7$. *Phys. Rev. B* **70**, 012402 (2004).
26. Petrenko, O. A., Lees, M. R. & Balakrishnan, G. Titanium pyrochlore magnets: how much can be learned from magnetization measurements? *J. Phys.* **23**, 164218 (2011).
27. Champion, J. D. M. et al. Order in the heisenberg pyrochlore: the magnetic structure of $Gd_2Ti_2O_7$. *Phys. Rev. B* **64**, 140407 (2001).
28. Stewart, J. R., Ehlers, G., Wills, A. S., Bramwell, S. T. & Gardner, J. S. Phase transitions, partial disorder and multi- k structures in $Gd_2Ti_2O_7$. *J. Phys.* **16**, L321 (2004).
29. Kouvel, J. & Kasper, J. Long-range antiferromagnetism in disordered FeNiMn alloys. *J. Phys. Chem. Solids* **24**, 529 – 536 (1963).
30. Kamiya, Y. & Batista, C. D. Magnetic vortex crystals in frustrated mott insulator. *Phys. Rev. X* **4**, 011023 (2014).
31. Janssen, L., Andrade, E. C. & Vojta, M. Honeycomb-lattice Heisenberg−Kitaev model in a magnetic field: spin canting, metamagnetism, and vortex crystals. *Phys. Rev. Lett.* **117**, 277202 (2016).
32. Li, B. et al. Competing magnetic interactions in the antiferromagnetic topological insulator $MnBi_2Te_4$. *Phys. Rev. Lett.* **124**, 167204 (2020).
33. Puphal, P. et al. Topological magnetic phase in the candidate weyl semimetal CeAlGe. *Phys. Rev. Lett.* **124**, 017202 (2020).
34. Gao, S. et al. Fractional antiferromagnetic skyrmion lattice induced by anisotropic couplings. *Nature* **586**, 37–41 (2020).
35. Glazkov, V. N. et al. Single-ion anisotropy and transverse magnetization in the frustrated gadolinium pyrochlores. *J. Phys.* **19**, 145271 (2007).
36. Petrenko, O. A., Lees, M. R., Balakrishnan, G., Glazkov, V. N. & Sosin, S. S. Magnetic phases in a $Gd_2Ti_2O_7$ pyrochlore for a field applied along the [100] axis. *Phys. Rev. B* **85**, 180412 (2012).
37. Ruff, J. P. C. et al. Spin waves and quantum criticality in the frustrated *xy* pyrochlore antiferromagnet $Er_2Ti_2O_7$. *Phys. Rev. Lett.* **101**, 147205 (2008).
38. Cracknell, A. P., Davies, B. L., Miller, S. C. & Love, W. F. *Kronecker Product Tables. General Introduction and Tables of Irreducible Representations of Space Groups*, Vol. 1 (Plenum, 1979).
39. Campbell, B. J., Stokes, H. T., Tanner, D. E. & Hatch, D. M. *ISODISPLACE*: a web-based tool for exploring structural distortions. *J. Appl. Crystallogr.* **39**, 607–614 (2006).
40. Stokes, H. T., Hatch, D. M. & Campbell, B. J. Isotropy software suite, iso.byu.edu.
41. Paddison, J. A. M. et al. Nature of partial magnetic order in the frustrated antiferromagnet $Gd_2Ti_2O_7$. Preprint at https://arxiv.org/abs/1506.05045 (2015).
42. Glazkov, V. N. et al. Single-ion anisotropy in the gadolinium pyrochlores studied by electron paramagnetic resonance. *Phys. Rev. B* **72**, 020409 (2005).
43. Fischer, H. E. et al. D4c: A very high precision diffractometer for disordered materials. *Appl. Phys. A* **74**, s160–s162 (2002).
44. Petrenko, O. & Fischer, H. E.PDF analysis of the Gd containing magnets. Institut Laue – Langevin (ILL) https://doi.org/10.5291/ill-data.easy-293
45. Paddison, J. A. M. et al. Spin correlations in the dipolar pyrochlore antiferromagnet $Gd_2Sn_2O_7$. *J. Phys* **29**, 144001 (2017).
46. Ibberson, R., David, W. & Knight, K. The high-resolution powder diffractometer (HRPD) at ISIS–a user guide. Tech. Rep., RAL (1992).
47. Ibberson, R. M. Design and performance of the new supermirror guide on HRPD at ISIS. *Nucl. Instr. Meth. Phys. Res. A* **600**, 47–49 (2009).
48. Ehlers, G. Study of slow dynamic processes in magnetic systems by neutron spin-echo spectroscopy. *J. Phys.* **18**, R231 (2006).
49. Brenig, W. & Chernyshev, A. L. Highly dispersive scattering from defects in noncollinear magnets. *Phys. Rev. Lett.* **110**, 157203 (2013).
50. Jensen, J. & Bak, P. Spin waves in triple-$\vec{q}$ structures. Application to USb. *Phys. Rev. B* **23**, 6180–6183 (1981).
51. Longfield, M. J., Paixão, J. A., Bernhoeft, N. & Lander, G. H. Resonant x-ray scattering from multi-**k** magnetic structures. *Phys. Rev. B* **66**, 054417 (2002).
52. Marcus, G. G. et al. Multi-*q* mesoscale magnetism in $CeAuSb_2$. *Phys. Rev. Lett.* **120**, 097201 (2018).
53. Balakrishnan, G., Petrenko, O. A., Lees, M. R. & Paul, D. M. Single crystal growth of rare earth titanate pyrochlores. *J. Phys.* **10**, L723 (1998).
54. Gardner, J. S., Gaulin, B. D. & Paul, D. M. Single crystal growth by the floating-zone method of a geometrically frustrated pyrochlore antiferromagnet, $Tb_2Ti_2O_7$. *J. Cryst. Growth* **191**, 740 – 745 (1998).
55. Chapon, L. C. et al. Wish: the new powder and single crystal magnetic diffractometer on the second target station. *Neutron N.* **22**, 22–25 (2011).
56. Copley, J. R. D. & Cook, J. C. The disk chopper spectrometer at NIST: a new instrument for quasielastic neutron scattering studies. *Chem. Phys.* **292**, 477–485 (2003).
57. Coelho, A. A.*Topas Academic: General Profile and Structure Analysis Software for Powder Diffraction Data, version 5* (2012).

58. Toth, S. & Lake, B. Linear spin wave theory for single-*q* incommensurate magnetic structures. *J. Phys.* **27**, 166002 (2015).

ACKNOWLEDGEMENTS

We are grateful to A.T. Boothroyd, S.T. Bramwell, M.J. Cliffe, M.J.P. Gingras, P. McClarty, M. Mourigal, P.J. Saines, and A.S. Wills for useful discussions, to O. Kirichek and the ISIS Sample Environment Group for cryogenic support, and to J. Makepeace and M.S. Senn for assistance with TOPAS 5. J.A.M.P.'s work was supported by the Laboratory Directed Research and Development Program of Oak Ridge National Laboratory, managed by UT-Battelle, LLC for the US Department of Energy (manuscript preparation). J.A.M.P.'s work at Cambridge (magnetic structure analysis) was supported by Churchill College, University of Cambridge. J.A.M.P., A.B.C., and A.L.G. acknowledge financial support from the STFC, EPSRC (EP/G004528/2), and ERC (Ref: 279705). A portion of this research used resources at the Spallation Neutron Source, a DOE Office of Science User Facility operated by the Oak Ridge National Laboratory. Work at NHMFL (H.D.Z.) was supported by the NSF-DMR-1157490 and the State of Florida and U.S. Department of Energy. Experiments at the ISIS Neutron and Muon Source were supported by a beam time allocation from the STFC (U.K.). This manuscript has been authored by UT-Battelle, LLC under Contract No. DE-AC05-00OR22725 with the U.S. Department of Energy. The United States Government retains and the publisher, by accepting the article for publication, acknowledges that the United States Government retains a non-exclusive, paid-up, irrevocable, world-wide license to publish or reproduce the published form of this manuscript, or allow others to do so, for United States Government purposes. The Department of Energy will provide public access to these results of federally sponsored research in accordance with the DOE Public Access Plan (http://energy.gov/downloads/doe-public-access-plan).

AUTHOR CONTRIBUTIONS

J.A.M.P. wrote the manuscript and analyzed magnetic neutron-diffraction data. A.B.C. analyzed neutron-diffraction data (HRPD instrument). J.A.M.P., G.E., J.S.G., O.A.P., N.P.B., D.D.K., P.M., H.E.F., and J.R.S. performed neutron-scattering experiments. J.S.G. prepared the polycrystalline sample and H.Z. prepared the single-crystal sample. A.L.G., D.D.K., and P.M. oversaw crystallographic analysis. J.R.S. devised the project, performed neutron-scattering experiments, and analyzed inelastic neutron-scattering data.

COMPETING INTERESTS

The authors declare no competing interests.

ADDITIONAL INFORMATION

Supplementary information The online version contains supplementary material available at https://doi.org/10.1038/s41535-021-00391-w.

Correspondence and requests for materials should be addressed to Joseph A. M. Paddison or J. Ross Stewart.

Reprints and permission information is available at http://www.nature.com/reprints

Publisher's note Springer Nature remains neutral with regard to jurisdictional claims in published maps and institutional affiliations.